photonics

MDPI

Article

Modeling the Electro-Optical Performance of High Power Mid-Infrared Quantum Cascade Lasers

Hans Dieter Tholl [1,*], Quankui Yang [2] and Joachim Wagner [2]

[1] Diehl BGT Defence, Alte Nussdorfer Strasse 13, Überlingen 88662, Germany
[2] Fraunhofer Institute for Applied Solid State Physics, Tullastrasse 72, Freiburg 79108, Germany; quankui.yang@iaf.fraunhofer.de (Q.Y.); joachim.wagner@iaf.fraunhofer.de (J.W.)
* Correspondence: hans.tholl@diehl-bgt-defence.de; Tel.: +49-7551-89-4224

Received: 24 March 2016; Accepted: 10 May 2016; Published: 17 May 2016

Abstract: Performance modeling of the characteristics of mid-infrared quantum cascade lasers (MIR QCL) is an essential element in formulating consistent component requirements and specifications, in preparing guidelines for the design and manufacture of the QCL structures, and in assessing different modes of operation of the laser device. We use principles of system physics to analyze the electro-optical characteristics of high power MIR QCL, including thermal backfilling of the lower laser level, hot electron effects, and Stark detuning during lasing. The analysis is based on analytical modeling to give simple mathematical expressions which are easily incorporated in system-level simulations of defense applications such as directed infrared countermeasures (DIRCM). The paper delineates the system physics of the electro-optical energy conversion in QCL and the related modeling. The application of the performance model to a DIRCM QCL is explained by an example.

Keywords: quantum cascade lasers; performance modeling; directed infrared countermeasures

1. Introduction

Quantum cascade lasers (QCL) provide direct generation of mid-infrared radiation for several airborne applications. Especially high-power QCL could replace diode-pumped solid state lasers coupled to optical parametrical generators/oscillators (OPG/OPO) in directed infrared countermeasure (DIRCM) systems because they show reduced complexity with much fewer parts to be assembled, exhibit smaller mass and volume, and may be less expensive in investment and installation costs.

Changing an established and qualified laser technology in airborne systems requires a significant improvement in wallplug efficiency in order to reduce the required prime power from the platform. It is expected that maximizing the wallplug efficiency also leads to increased optical output power without impacting the beam quality. At the system level, wallplug efficiency of a laser is primarily determined by the efficiency of the power supply module which converts and filters the platform input power, and by the heat removal subsystem. Moving from optically-pumped solid state/OPO laser systems to electrically-pumped QCL is one way to reduce the heat load. Another important factor is the improvement of the electro-optical efficiency, especially to bring the operating point of maximal electro-optical efficiency as close as possible to the point of maximal optical output power.

An essential element in the assessment of the electro-optical performance of lasers in different applications is modeling using a system physics approach [1]. System physics uses conservation laws complemented with constitutive equations relating observable fluxes (currents) to driving forces (potential differences) representing physical processes. An early application of system physics is the engineering of heat engines. Central to the modeling of these engines are the energy conservation law and the related efficiencies of the conversion processes between different forms of energy. The laser, considered as a light engine, fits very well into this framework. From the point of view of a system-level assessment of QCL, modeling based on solving the Schrödinger equation, to use a density matrix formalism, employing non-equilibrium Green's function formalism, or Monte Carlo simulations, to name a few examples [2–4], are not very helpful because they require complex calculations and detailed knowledge of the values of quantum level parameters which are not readily available.

Recently, models describing the performance of QCL using efficiencies [5–8], an approach well known from solid state laser engineering [9], have been proposed. They deal with QCL in the vicinity of the lasing threshold, taking into account the escape of electrons from the upper laser level and thermal backfilling of the lower laser level from the injector. In directed infrared countermeasures applications we operate the QCL at high optical power levels and, consequently, high pump currents. Stark detuning of the energy levels, the subsequent decrease in the oscillator strength of the laser transition, and the reduction of the injection efficiency from the injector into the upper laser level cannot be neglected in devices operating near the maximum current the structure can sustain.

This paper deals with the modeling of the optical output power *vs.* pump current of high-power mid-infrared QCL taking thermal backfilling, hot electrons, and Stark detuning into account. The purpose of the modeling is the assessment of the electro-optical performance in different modes of operation of the laser device, the formulation of consistent component requirements and specifications, and the preparation of guidelines for the design and manufacture of the QCL structures to meet the specified performance goals.

The subject matter of the paper is outlined as follows: The first two sections introduce the electro-optical energy conversion processes, the electro-optical performance model, its descriptors and observables. Then, the model is compared to experimental data. The conclusion highlights the applicability of the model to represent the performance of mid-infrared QCL on a system level.

2. Electro-Optical Energy Conversion in MIR Quantum Cascade Lasers

The quantum cascade laser is a semiconductor laser employing a unipolar (electron) current to convert electricity into optical energy. The electro-optical architecture of a QCL can be described as a cascade of gain stages which convert electrical energy into coherent optical energy (work) and heat when pumped above the laser threshold. Figure 1 depicts a sketch of a simplified energy level diagram of a single stage of the quantum cascade. The electron flow leading to the electro-optical energy conversion is drawn in red. The blue arrows represent non-radiative transitions of the electrons. The cascade is embedded in a waveguide, which defines the optical modes and also serves as resonator. The physical principles underlying the conversion process are similar to the quasi three-level laser scheme well known in solid state laser physics. In this scheme, the ground state of the QCL (level 0) is the lowest state in a manifold of sublevels (comprising level 1 and the injector) which are coupled among each other and to the lower laser state (level 2). Consequently, the lower laser state is always populated with electrons and the laser behaves in a way which is intermediate between a three-level (levels 0, 2, and 3) and a four-level (levels 0, 1, 2, and 3) laser. This backfilling of electrons is controlled by the energy difference Δ_{inj} between the lower laser state (level 2) and the ground state (level 0). In addition, there is an excited state manifold (indicated as level 4 in Figure 1) into which electrons from the upper laser state (level 3) can escape and bypass the laser transition.

Above the lasing threshold, the difference in electron population between the upper and the lower laser state is clamped at its threshold value. Please note, that the population inversion between the laser states is constant during operation but not the electron density in the upper laser state, as in bipolar semiconductor lasers.

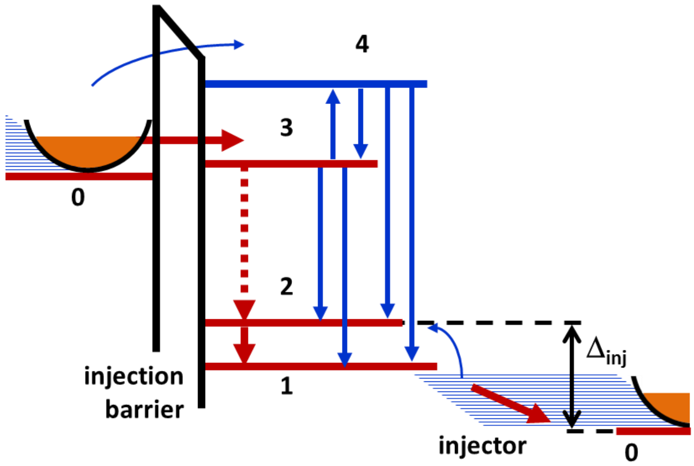

Figure 1. Simplified energy level diagram of a single gain stage of the quantum cascade involved in the electro-optical energy conversion. The electron flow leading to the electro-optical energy conversion is drawn in red. Stimulated photon emission is represented by the broken arrow connecting levels 3 and 2. The blue arrows represent non-radiative transitions of the electrons. The in-plane kinetic energy distribution of the ground state of the injector is indicated by the bowl-like pictogram.

The energy structure of a QCL is designed with a constant average voltage V_{fb} applied across the cascade. At this so-called flat-band voltage the ground state of the injector of one gain stage is energetically-aligned (in resonance) with the upper laser level of the succeeding stage. Its value can be easily estimated from Figure 1:

$$V_{fb} = N_c \cdot \left(\frac{\hbar\omega}{e} + \Delta_{inj} \right) \tag{1}$$

In the formula N_c is the number of gain stages (periods) and ω is the angular laser frequency defined by the energy spacing between the upper and the lower laser state, $\hbar$ is the reduced Planck constant, and e is the unit electron charge $\left(= 1.6 \times 10^{-19}\ \mathrm{As}\right)$.

In operation, the QCL is pumped electrically by a current I and the quantum cascade is aligned by applying a voltage U across the device. At the lasing threshold, the (internal) voltage across the cascade is equal to:

$$V_{th} = U_{th} - R_s \cdot I_{th} \tag{2}$$

In the formula, R_s is the series resistance of the cladding layers and the contacts, U_{th} and I_{th} are the applied voltage and the current at the threshold. During lasing, the voltage across the cascade remains clamped at V_{th} because the current is driven by stimulated emission of [10].

The energy conversion within the quantum cascade can be expressed as a balance equation of the form [1]:

$$V_{th} \cdot I = \frac{V_{th} \cdot I_s}{\eta_i} + \frac{P}{\eta_V \cdot \eta_L} \tag{3}$$

The pump current I generates heat (loss current I_s) and photons with an optical power P. The injection efficiency η_i is the ratio of the number of electrons injected from the injector into the upper laser state and the number of electrons introduced into the cascade. The external quantum efficiency η_L is the number of photons per gain stage leaving the QCL resonator divided by the number of electrons injected above threshold. The ratio η_V is equal to the photon energy divided by the energy loss of the electrons per gain stage:

$$\eta_V = \frac{N_c \cdot \hbar\omega}{e \cdot V_{th}} \tag{4}$$

The basic physical processes supporting the quasi-three-level laser scheme of the conversion of electrical into optical energy in MIR QCL are the following [3]:

- Pumping of the active region through voltage controlled resonant tunneling of electrons from the ground state (0) of the injector into the upper laser state (level 3) through an injection barrier;
- Photon driven relaxation of electrons from the upper (level 3) to the lower (level 2) laser state;
- Depletion of the lower laser state (level 2) by longitudinal optical (LO) phonon-driven relaxation of electrons into the upper state (level 1) of the injector manifold;
- Thermal backfilling of electrons from the injector into the lower laser state (level 2) mediated by LO phonon reabsorption; and
- Transport of electrons through the injector in terms of sequential transitions from the upper injector state (level 1) to its ground state.

The effectiveness of the energy conversion process is reduced by additional processes:

- Escape of electrons from the upper laser state (level 3) into states lying energetically higher and subsequent relaxation into lower lying states essentially by-passing the laser process [5,6];
- Stark detuning of the energy levels with respect to the flat-band design resulting in a decrease of the oscillator strength of the laser transition and in a reduction of the injection efficiency into the upper laser level due to the opening of additional non-resonant transitions to other states in the active region or into the continuum [11]; and
- Heating of the electrons above the lattice temperature [12].

There are other relevant processes which can affect the energy conversion efficiency in mid-infrared QCL such as free-carrier absorption or interface-roughness scattering. We assume that these effects are implicitly represented in the parameters values specifying the threshold current density and the optical gain.

3. Electro-Optical Performance Model

The electro-optical performance model relates the stationary photon sheet density S (photons/cm^2) per gain stage to the pump current density J (kA/cm^2). All sheet densities are referred to the area of the resonator waveguide perpendicular to the current flow.

3.1. Population Inversion, Gain, and Photon Sheet Density in MIR QCL

The starting point for the electro-optical performance model is the population inversion Δn between the two laser states with electron sheet densities n_3 and n_2 (electrons/cm^2) per gain stage. The population inversion is written in a form known from solid state laser physics [9]:

$$\Delta n = n_3 - (\chi_i - 1) \cdot n_2 \tag{5}$$

In solid state lasers the (dimensionless) inversion reduction factor χ_i is related to the ratio of the emission and of the absorption cross sections of the two laser states ([9], p. 24). In QCL, χ_i represents the influences of the non-parabolicity of the in-plane motion of the electrons and of the second-order scattering-assisted optical transition between the laser subbands on the population inversion ([3], p. 238).

Within the k-th gain stage, we model the dependence of the population inversion Δn on the sheet density r_p of the pumping rate (transitions/s/cm^2) and on the photon sheet density S by considering the balance between pumping, depletion by stimulated emission, and thermal backfilling from the injector manifold as follows:

$$\Delta n_{(k)} = \left(\tau_{eff} \cdot r_p\right)_{(k)} - \left(\tau_{sat} \cdot \Gamma \cdot \sigma_e \cdot \Delta n \cdot S \cdot c_g\right)_{(k)} - \left[(\chi_i - 1) \cdot n_{therm}\right]_{(k)} \tag{6}$$

The effective transition time between the laser levels τ_{eff} and the relaxation time τ_{sat} (which is related to the photon saturation sheet density) depend on the electron temperature T_e and on the lattice temperature T_L, which are controlled by the pumping current density J.

The other symbols represent the overlap factor Γ of the waveguide mode with the active region of k-th gain stage, the population inversion threshold n_{therm} caused by thermal backfilling of electrons from energy states below the lower laser state, and the group velocity c_g of energy transport in the optical mode.

The average gain coefficient γ (1/cm) per gain stage is defined by $\gamma = \frac{1}{N_c}\sum_{k=1}^{N_c}(\sigma_e \Delta n)_{(k)}$. In the expression, σ_e (cm) is the emission "cross-section" of the upper laser level. The summation symbol comprises any inhomogeneous broadening of the optical transition. For simplicity, we assume a homogeneous linewidth and uniform gain stages. Thus, we can write:

$$\gamma = \sigma_e \cdot \tau_{eff} \cdot r_p - \gamma \cdot \frac{S}{S_{sat}} - \alpha_{therm} \tag{7}$$

The saturation value of the photon sheet density is defined by $S_{sat} = 1/\left(\Gamma_m \sigma_e \tau_{sat} c_g\right)$, the mean overlap factor per gain stage is $\Gamma_m = \frac{1}{N_c}\sum_{k=1}^{N_c}\Gamma_{(k)}$, and $\alpha_{therm} = \sigma_e\left(\chi_i - 1\right) n_{therm}$ (1/cm) is an effective loss coefficient describing the reduction of population inversion due to thermal backfilling.

Above the lasing threshold, the gain is clamped at its threshold value γ_{th} and the equation can be solved for the photon sheet density:

$$S = S_{sat} \cdot \frac{\gamma_p - (\gamma_{th} + \alpha_{therm})}{\gamma_{th}} \tag{8}$$

We have introduced the small signal gain coefficient $\gamma_p = \sigma_e \tau_{eff} r_p$. Lasing occurs if γ_p exceeds the effective threshold value $\gamma_s = \gamma_{th} + \alpha_{therm}$.

To proceed, we require an expression relating γ_p to the pump current density. Near the threshold, a popular assumption is $r_p = J/e$, resulting in a linear dependence of the form $\gamma_p = \sigma_e\ \tau_{eff}\ J/e$.

For high power MIR QCL this assumption is not valid. The large electric field associated with high current densities shifts the energy levels of the cascade relative to their design values. This Stark shift leads to a decrease in oscillator strength of the optical transition (affecting σ_e) and, more importantly, it opens up new non-resonant transitions to additional states in the active region or into the continuum. These new conductive channels reduce the efficiency of the electron injection from the injector into the upper laser level (affecting τ_{eff}). We model the pump process relating the gain γ_p and the current density J under the influence of the Stark detuning by introducing a second order term as follows:

$$\gamma_p(J) = g_c \cdot J \cdot \left(1 - \frac{J}{J_0}\right) \tag{9}$$

In the formula $g_c = \sigma_e \tau_{eff}/e$ is the differential gain for small pump current densities $J << J_0$. The parameter J_0 sets the scale for the Stark detuning of the energy levels in the cascade. We assume that the Stark scale J_0 is an intrinsic property of the quantum structure, independent of the electron temperature T_e.

With the model for the pump process of the active region we attain the following model equation for the photon sheet density after an elementary calculation (we tacitly assume throughout the paper that $S \geqslant 0$):

$$S = \frac{S_{sat} \cdot \left(\gamma_{th} + \alpha_{therm}\right)}{\gamma_{th}} \cdot \left(\frac{J}{A} - 1\right) \cdot \left(1 - \frac{J}{B}\right) \tag{10}$$

The coefficients A and B are defined as follows:

$$A = \frac{2\left(\gamma_{th} + \alpha_{therm}\right)}{g_c \cdot \left(1 + \sqrt{1 - \frac{4(\gamma_{th} + \alpha_{therm})}{g_c \cdot J_0}}\right)} \tag{11}$$

and:

$$B = \frac{2\left(\gamma_{th} + \alpha_{therm}\right)}{g_c \cdot \left(1 - \sqrt{1 - \frac{4(\gamma_{th} + \alpha_{therm})}{g_c \cdot J_0}}\right)} \tag{12}$$

The A-coefficient determines the lasing threshold. For high current densities $J > B$ the photon emission is quenched due to the Stark detuning of the energy levels. The sum of both coefficients equals the Stark scale: $A + B = J_0$. In general, A and B depend on the electron temperature and on the lattice temperature. Both temperatures depend on the pump current density so that the photon sheet density S is only formally a quadratic function of J, as will be shown in the next subsection.

3.2. Dealing with Hot Electrons and Stark Detuning

The following procedure is adopted to deal with the hot electrons and Stark detuning in MIR QCL. We assume that the dependences of the coefficients A and B on the electron temperature are approximated by linear functions. In particular, we make the following substitution for $A(T_e, T_L)$:

$$A\left(T_e, T_L\right) = \frac{J_s}{1 - \varepsilon_s} + \varepsilon_h \cdot \left(T_e - T_L\right) \tag{13}$$

The meanings of J_s, ε_s, and ε_h will be explained below. The thermal model given in [12] provides an expression for the temperature difference: $T_e - T_L = \alpha_{EL}\, J$. The parameter α_{EL} describes the thermal coupling of the electrons to the lattice. In MIR QCL based on the GaInAs/AlInAs/InP material system we assume a constant value of $\alpha_{EL} = 35$ Kcm^2/kA [12] discarding the dependence of α_{EL} on the particular device structure and operating condition.

The linear approximation for the coefficient $B\left(T_e, T_L\right)$ is easily derived on the basis of the relation $A + B = J_0$ and the assumption that J_0 is independent of the electron temperature:

$$B\left(T_e, T_L\right) = \frac{J_s}{\varepsilon_s} - \varepsilon_h \cdot J \tag{14}$$

In the linear approximation of the coefficients A and B, the photon sheet density S depends on the three quantities: J_s, ε_s, and ε_h, which control the operation of the QCL.

The *loss current density*

$$J_s\left(T_L\right) = \left(\frac{\gamma_{th} + \alpha_{therm}}{g_c}\right)_{T_e = T_L} \tag{15}$$

equals the threshold current of the QCL structure in the particular case defined by thermal equilibrium between the electrons and the lattice, thermal backfilling at the lattice temperature, and operation at the flat-band voltage (quasi-three-level lasing scheme).

The *Stark loss factor*

$$\varepsilon_s(T_L) = \frac{1}{2}\left(1 - \sqrt{1 - \frac{4\, J_s}{J_0}}\right) \tag{16}$$

is derived by setting $T_e = T_L$ in Equation (11) and by introducing J_s from Equation (15). This factor describes the reduction of the efficiency of electron injection from the injector into the upper laser state and the decrease in oscillator strength of the laser transition due to the Stark detuning of the energy levels. It will be shown below that the *Stark scale* J_0 is equal to two times the value of the roll over current density J_{ro} of the P-I curve. The dependence of ε_s on this ratio is depicted in Figure 2a.

The *heating loss factor*

$$\varepsilon_h\left(T_L\right) = \alpha_{EL} \cdot \left(\frac{dA}{dT_e}\right)_{T_L} \tag{17}$$

is a measure for the loss of pump energy due to the heating the electrons above the lattice temperature. In order to estimate the order of magnitude of the heating loss factor we generated a dependence on the electron temperature for the gain cross-section σ_e and the inversion reduction factor χ_i using the non-parabolic subbands theory of [13]. The thermal backfilling loss coefficient α_{therm} was calculated according to [14] with the lattice temperature replaced by the electron temperature. With the help of a 4-level rate equation model [15] including electron escape from the upper laser level along the lines of [6,7] we generated the coefficient $A\,(T_e, T_L)$ and calculated the derivative $(dA/dT_e)_{T_L}$ numerically for different QCL structures. A result of these calculations is shown in panel of Figure 2b. The ε_h values span a range between 0% and 20% depending on the lattice temperature and on the value of the Stark current scale J_0.

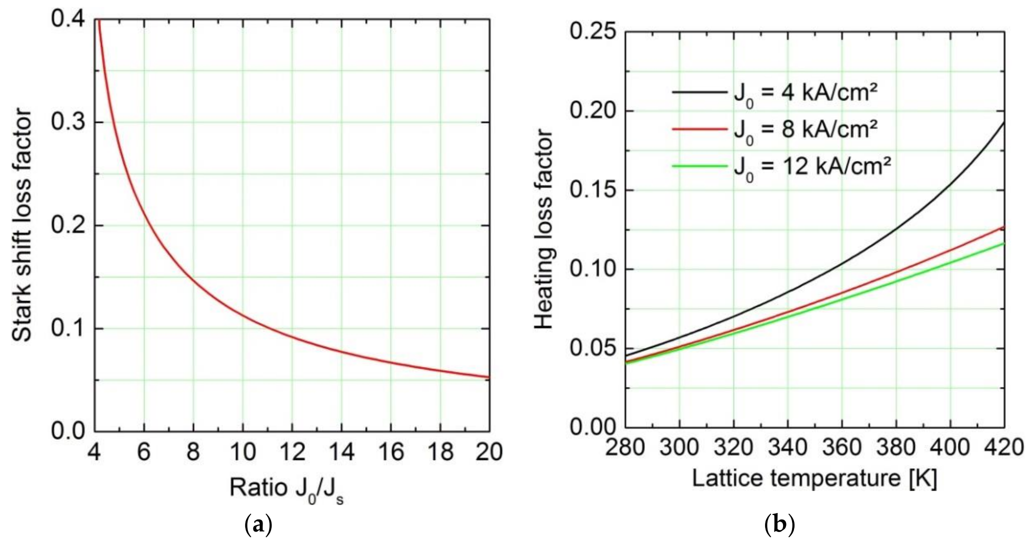

Figure 2. Loss factors. (**a**) Stark loss factor ε_s as a function of the ration J_0/J_s; and (**b**) electron heating loss factor ε_h as a function of the lattice temperature for different Stark scales J_0.

The Stark current scale is the parameter which drives the QCL electro-optical performance. A small value of J_0 leads to the occurrence of the Stark roll-over within the dynamic current range of the device (in a pulsed low duty cycle mode). Ideally, the value of the Stark current scale is well beyond the maximum current determined by the doping level of the device. A preliminary evaluation [15] of measured data (from the author's labs and from publications) using the model indicates that the ratio J_0/J_s assumes values between 6 and 10. Therefore, we expect ε_s to take on values between 10% and 20% and ε_h to be in the order of a few percent. A detailed assessment of the application of the model to QCL devices is the topic of an ongoing study and beyond the scope of this paper.

3.3. Threshold Current Density

The threshold current density for *constant lattice temperature* (which happens in short pulse low duty cycle operation of the QCL) is defined by the onset of photon emission, *i.e.*,:

$$J_{th} = A\,(T_e\,(J_{th})\,, T_L) \tag{18}$$

This is an implicit equation for the calculation of J_{th}. We solve this equation using the linear approximation for $A\,(T_e, T_L)$ derived above. The result is:

$$J_{th} = \frac{J_s}{(1-\varepsilon_h)\cdot(1-\varepsilon_s)} \tag{19}$$

The threshold current density J_{th} of the device is larger than the loss current density J_s because pump energy is lost to the heating of the electrons (factor ε_h) and to the Stark shift of the energy levels (factor ε_s). The product $\eta_i\,(J_{th}) = (1-\varepsilon_h)\,(1-\varepsilon_s)$ can be interpreted as the efficiency of the electron injection from the ground state of the injector into the upper laser level at the threshold.

Looking at the equation for the threshold current density, we see that the well-known procedure of estimating the waveguide losses by fitting a straight line to the dependence of J_{th} on $1/L_R$ needs to be interpreted carefully in order to separate the contributions of device losses, thermal backfilling, hot electrons, and Stark detuning.

3.4. Quenching Current Density

At *constant lattice temperature*, the laser stops the emission of photons if the pump current density exceeds the current density J_q defined implicitly by the equation $J_q = B\left(T_e\left(J_q\right), T_L\right)$. In linear approximation we attain the solution:

$$J_q = \frac{J_s}{(1+\varepsilon_h)\cdot\varepsilon_s} \tag{20}$$

The quenching current density J_q depends strongly on the loss parameter ε_s and is, thus, directly related to the Stark detuning of the energy levels. If the Stark detuning is negligible, the quenching current density becomes infinite and the photon sheet density grows until the maximum current density that the cascade can support is reached. If J_q is less than this maximum value, Stark roll-over limits the dynamic current range of the device measured by the difference $J_q - J_{th}$.

3.5. Electro-Optical Performance Model

Writing $A = J_{th} + \varepsilon_h (J - J_{th})$ and $B = J_q + \varepsilon_h \left(J_q - J\right)$ and rearranging the formula for the photon sheet density leads to the following expression for S which is valid for moderate heating loss factors ε_h:

$$S = S_{sat}\cdot \frac{g_c}{\gamma_{th}}\cdot \eta_h\cdot \eta_i(J)\cdot \left(1-\frac{J}{J_q}\right)\cdot (J - J_{th}) \tag{21}$$

The heating loss parameter ε_h reduces the photon sheet density through the efficiency factor:

$$\eta_h = 1 - \varepsilon_h \tag{22}$$

In addition, the heating of the electrons leads to a limitation of the photon sheet density at high pump current values. Suppressing the Stark shift by imposing $\varepsilon_s = 0$ gives the upper limit:

$$S_{upl} = S_{sat}\cdot \frac{g_c J_s}{\gamma_{th}}\cdot \left(\frac{1}{\varepsilon_h} - 1\right) \tag{23}$$

A second reduction factor of the photon sheet density is given by:

$$\eta_i(J) = \frac{(1-\varepsilon_h)\cdot(1-\varepsilon_s)}{1+\varepsilon_h\cdot\left(\frac{J}{J_{th}}-1\right)} \tag{24}$$

This factor represents the efficiency of the injection of electrons from the injector into the upper laser level. At threshold, η_i is equal to $\eta_i(J_{th}) = (1-\varepsilon_h)(1-\varepsilon_s)$.

Finally, the factor $1 - J/J_q$ parameterizes the quenching of the photon emission due to the reduction of the dynamic current range.

The photon sheet density S given in Equation (21) is a non-linear function of the current density J. The slope factor dS/dJ is determined (among other factors) by the escape of electrons from the upper laser state due to heating (factor ε_h) and by the Stark detuning (factor ε_s). These factors influence the slope already near the threshold. With increasing current density the heating factor η_h remains constant, whereas the injection efficiency η_i is reduced. In addition, hot electrons and Stark detuning reduce the dynamic range of the pump current through the factor $1 - J/J_q$.

The dependences of the reduction factors $\eta_i(J)$ and $1 - J/J_q$ on the normalized current density are depicted in Figure 3 for different values of ε_h and ε_s. The graphs show that for moderate values of ε_h and ε_s a reduction of the photon sheet density down to 50% of the value without considering heating and Stark detuning can be expected.

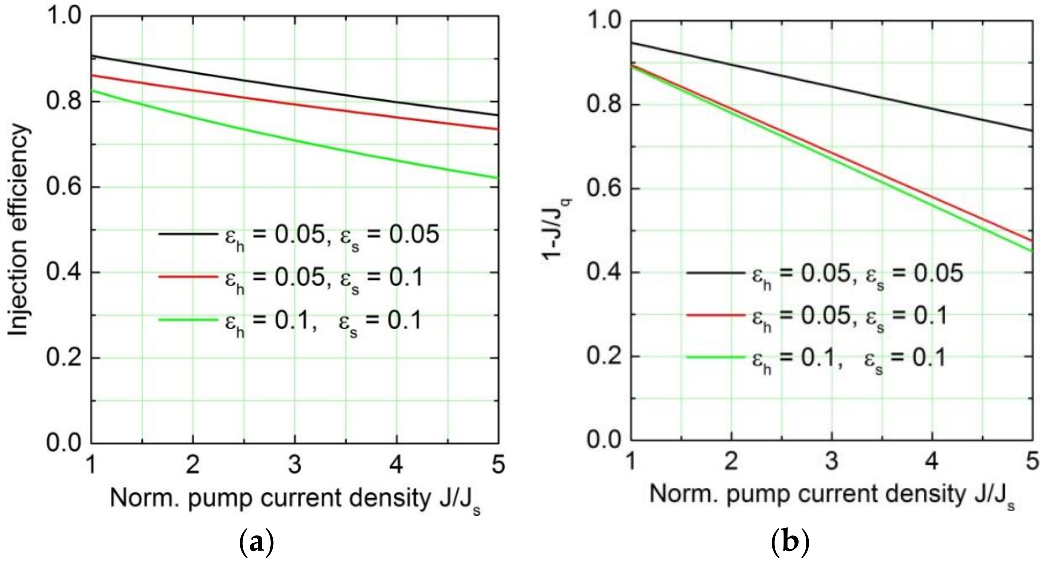

Figure 3. (**a**) Injection efficiency η_i and (**b**) quenching factor $1 - J/J_q$ as functions of the current density ratio J/J_s for different values of ε_h and ε_s.

The photon sheet density exhibits a maximum and may roll over with increasing current density, depending on the value of the Stark current scale J_0 (effective through ε_s). Roll-over occurs at the pump current density J_{ro} for which the slope dS/dJ equals zero. Differentiating the function $S(J)$ with respect to the pump current density J for a constant lattice temperature and performing an elementary calculation gives the formula:

$$J_{ro} = \frac{1}{2}\left(J_q + J_{th}\right) + \frac{J_{th}}{\varepsilon_h} \cdot \left[\sqrt{1 + \varepsilon_h\left(\frac{J_q}{J_{th}} - 1\right)} - \left(1 + \frac{\varepsilon_h}{2}\left(\frac{J_q}{J_{th}} - 1\right)\right)\right] \tag{25}$$

For small values of the heating loss ε_h the bracket on the right hand side is zero to first order. This implies that roll-over occurs approximately midway between the threshold and the quenching point: $J_{ro} \cong \frac{1}{2}\left(J_{th} + J_q\right)$. At the same order of approximation we have $J_0 \cong J_{th} + J_q$ which shows that the roll-over current density of the electro-optical characteristic is directly related to the Stark scale $J_{ro} \cong \frac{1}{2} J_0$.

Figure 4 depicts the non-linear dependence of the photon sheet density S on the normalized current density J/J_s. Panel (a) shows the influence of the hot electron factor ε_h on the roll-over of the electro-optical characteristics, panel (b) depicts the influence of the Stark detuning factor ε_s.

In practice, both mechanisms, *i.e.*, heating and Stark detuning, occur simultaneously. Figure 5 gives calculated electro-optical characteristics for different combinations of the loss parameters ε_h and ε_s. The Stark detuning factor ε_s determines primarily the position of the roll-over current (through J_0) whereas the heating factor ε_h adjusts the value of the photon sheet density at roll-over.

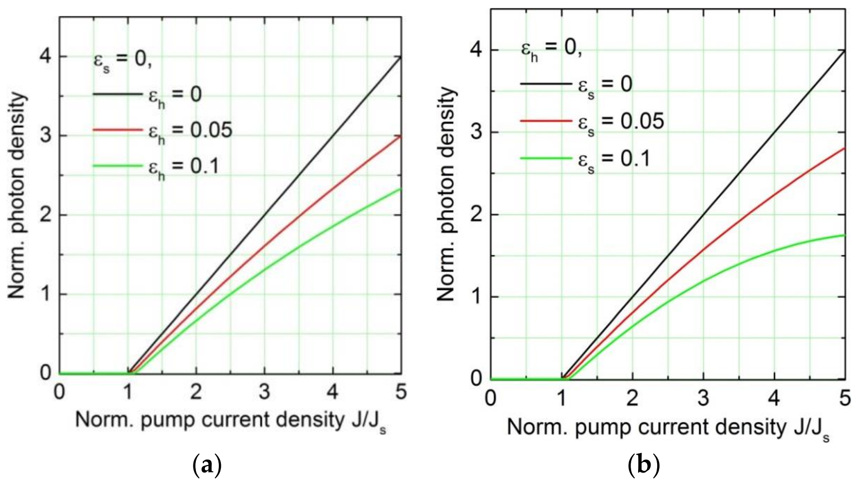

Figure 4. Photon sheet density as a function of the pump current density for various loss mechanisms. The photon sheet density is normalized to the value $S_{sat}\ g_c\ J_s/\gamma_{th}$. The pump current density is normalized by J_s. (**a**) Different values of the heating loss factor ε_h with suppressed Stark shift ($\varepsilon_s = 0$); (**b**) Different values of the Stark loss factor ε_s for thermal equilibrium of electrons and lattice ($\varepsilon_h = 0$).

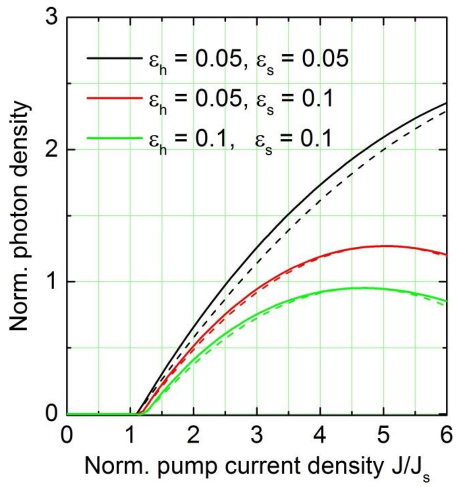

Figure 5. Photon sheet density as a function of the pump current density for various combinations of the loss parameters ε_h and ε_s.The photon sheet density is normalized to the value $S_{sat}\ g_c\ J_s/\gamma_{th}$. The pump current density is normalized by J_s. Solid curves are calculated with the performance model function, broken curves give the results for the parabolic approximation (Equation (26)).

3.6. Parabolic Approximation of the Optical Output Power Based on Observable Quantities

The expression for the photon sheet density given above depends on parameters which represent the internal mechanisms of the electro-optical energy conversion. This description is useful to guide design decisions, for example concerning the resonator geometry or facet coatings. For system level simulations we require model parameters which are observable at the device level. To arrive at such a model we introduce in Equation (21) the value of S at the roll-over point, $S_{ro} = S\,(J_{ro})$, replace J_q by the approximate value $J_q \cong J_0 - J_{th}$ and assume that $\eta_i\,(J)$ is roughly equal to its roll-over value $\eta_i\,(J_{ro})$. This procedure leads to a parabolic approximation of the dependence of the photon sheet density on the current density parameterized with the experimentally observable quantities J_{th}, S_{ro}, and J_0 ($\cong 2J_{ro}$ for constant T_L):

$$S\,(J) \cong \frac{4S_{ro}}{J_0 - 2J_{th}} \cdot \frac{J_0 - J_{th} - J}{J_0 - 2J_{th}} \cdot (J - J_{th}) \tag{26}$$

A comparison of the parabolic model function with the full performance model is depicted in Figure 5. It is evident that the parabolic approximation improves with increasing influence of the Stark roll-over for current densities between the threshold and the roll-over current density. In other words, this region is sufficiently well approximated using the parabolic model.

3.7. External Quantum Efficiency

Introducing the Equations (19), (22) and (23) into Equation (3) leads to the following expression of the conservation of energy within the quantum cascade above threshold:

$$V_{th} \cdot I = V_{th} \cdot I_{th} + V_{th} \cdot \varepsilon_h \cdot (I - I_{th}) + \cdot \frac{P}{\eta_V \cdot \eta_L} \tag{27}$$

The currents are given by expressions of the form $I = J\, L_R L_W$ where L_R and L_W are the length and the width of the resonator. The first and the second term of Equation (27) describe the heat generation in the cascade at the threshold and the additional heating of the electrons above the threshold.

Relating the output power P to the photon sheet density S through the mirror coupling loss α_M according to $P = \alpha_M \hbar\omega N_c S L_R L_W c_g$, substituting the photon sheet density S, and solving for the external quantum efficiency η_L leads to:

$$\eta_L = \frac{\alpha_M}{\alpha_M + \alpha_{AR}} \cdot \frac{\tau_{eff}}{\tau_{sat}} \cdot \eta_i(J) \cdot \left(1 - \frac{J}{J_q}\right) \tag{28}$$

with α_{AR} denoting the losses due to free electron absorption and optical losses in the resonator.

The external quantum efficiency η_L is different from the differential slope efficiency because the injection efficiency and the reduction of the dynamic range depend on the current density. The factor $\eta_i \left(1 - J/J_q\right)$ reduces the quantum efficiency relative to its value without hot electrons and Stark shift. This relative value is depicted in Figure 6 for different combinations of the loss parameters ε_h and ε_s. Even for moderate loss factors of 5% the reduction in quantum efficiency due to heating and Stark detuning is considerable.

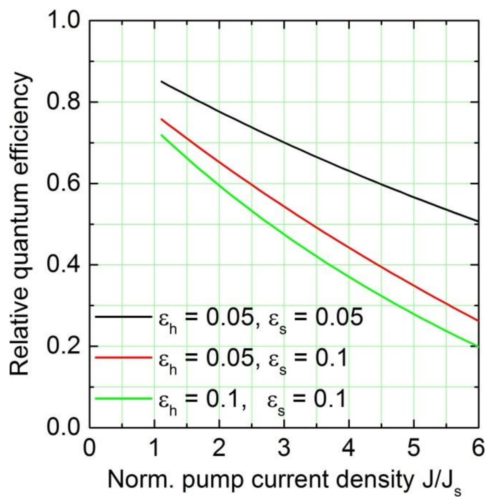

Figure 6. Relative quantum efficiency $\eta_i \left(1 - J/J_q\right)$ as a function of the pump current density for various combinations of the loss parameters ε_h and ε_s. Below the threshold the quantum efficiency is zero.

4. Experiments and Discussion

The electro-optical performance model relates the optical output power of a QCL to the pump current at a constant lattice temperature. The model can be used to characterize and to summarize the power characteristics of QCL grown and processed in a similar way for a specific application. The model parameters are established using a calibration procedure in pulsed mode operations. Once the model is set up, system simulations can be used to assess the performance of QCL in different modes of operation.

Especially useful for system-level calculations is the parabolic approximation with the directly observable parameters threshold current I_{th}, Stark scale current I_0, and output power P_{ro} at roll-over. The values of these parameters have to be measured in a pulsed low duty cycle mode of operation in order to avoid self-heating, and to keep the lattice temperature as close as possible to the heatsink temperature which can be controlled during the measurement. Stepping through the heatsink temperature and fitting the parabolic model at each step to the power-versus-current characteristics of the QCL under investigation gives three functions relating the model parameters to the heatsink temperature.

The usual procedure is to fit exponential functions to the temperature variation of these data: the threshold current increases as $I_{th}\left(T_L\right) = I_{th}\left(T_{ref}\right) \cdot \exp\left(\left(T_L - T_{ref}\right)/T_0\right)$, the optical power at roll-over decreases according to $P_{ro}\left(T_L\right) = P_{ro}\left(T_{ref}\right) \cdot \exp\left(\left(T_{ref} - T_L\right)/T_2\right)$, and the Stark scale decreases as $I_0\left(T_L\right) = I_0\left(T_{ref}\right) \cdot \exp\left(\left(T_{ref} - T_L\right)/T_3\right)$ over a (limited) temperature range of interest. In these empirical models it was assumed the lattice temperature equals the heat sink temperature ($T_L \cong T_{hs}$).

The calibration of the model parameters is completed by measuring the electro-optical characteristics of the QCL under pulse train pumping with different duty cycles. In this case the temperature of the lattice is greater than the temperature of the heat sink. Both temperatures can be related by a simple thermal model of the form $T_L = T_{hs} + \xi\, R_{LH}\, U\, I$ [3] to the electrical (pulse) power $U\, I$ and to the duty cycle ξ. Using curve-fitting techniques, the effective thermal resistance R_{LH} of the QCL structure may be estimated from the experimental data.

We demonstrate the application of the modeling approach for the characterization of 4.6 μm QCL devices using an experimental data set obtained from high-power MIR QCL developed at Fraunhofer IAF. The active region design of the QCL is based on a slightly-diagonal-transition [16]. After the material growth, the wafers were processed into mesa waveguide lasers by etching double trenches to define the ridges of about 12 μm in width. After processing, the wafers were cleaved into laser bars with cavity lengths of 3.5 mm, either leaving the facets uncoated for standard low duty-cycle characterization to obtain the characteristic temperature T_0, or high-reflectively (HR) coated on the back facet with R ~ 0.8 to enhance the light emission of the front facet for high duty-cycle operation as well as CW operation.

The lasers were soldered onto gold-plated copper heatsinks, either simply epilayer-up for low duty-cycle characterization, or epilayer-down after HR coating of the back facet for high duty-cycle or CW operation. After wire-bonding, the mounted devices were attached to a thermoelectric cooler for electrical and optical characterization. The temperature of the thermoelectric cooler was varied between 270 K and 360 K. For low duty-cycle operation, the lasers were driven by current pulses of 100 ns width at a repetition rate of 1 kHz to avoid accumulative self-heating of the devices. The emitted light was collimated by an F/1.6 off-axis parabolic mirror and focused either into a Fourier transform spectrometer (spectral resolution 0.1 cm^{-1}) equipped with a liquid-nitrogen cooled cadmium-mercury-telluride detector for characterization of the emission spectra, or onto a calibrated room-temperature pyro-electric detector for direct power measurement, while for high duty-cycle, the lasers were driven by current pulses of 300 ns width and repetition rates varying from 0.1 MHz to 2.5 MHz. For both high duty-cycle and CW operation, we placed a power meter directly in front of the emitting facet of the QCL chip, without any collection optics nor beam steering mirrors. The power meter has a diameter of 2 inches and the distance between the power meter and the laser front facet is about 1 cm, resulting in a collection solid angle of around 1.8π and ensuring almost 100% collection efficiency.

Figure 7 shows the optical power *vs.* pump current (P-I) curves in pulsed low duty cycle mode for a QCL chip with the dimension of 12 μm × 3.5 mm at various heat sink temperatures. The panel (a) gives the experimental data, the panel (b) shows the parabolic model (Equation (26)) fitted to the data. The model represents the experimental data with reasonable quality for the purpose of system-level simulations.

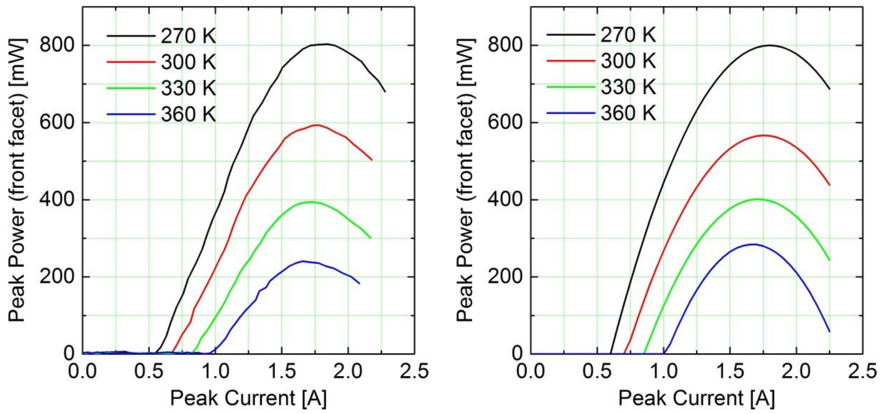

Figure 7. Peak optical output power *vs.* current amplitude in pulsed low duty cycle mode for various heat sink temperatures. Optical power from only the front facet has been counted; the total output power should be double of that when both facets are taken into account. The laser is driven by current pulses of 100 ns with a repetition rate of 1 KHz. (**a**) Experimental data; and (**b**) parabolic model fitted to the data.

The dependences of the threshold current, of the optical power at roll-over, and of the Stark scale on the heat sink temperature have been approximated with exponential functions. The model parameters are as follows for a reference temperature of $T_{ref} = 270$ K: $I_{th}\left(T_{ref}\right) = 0.60$ A, $T_0 = 170$ K; $P_{ro}\left(T_{ref}\right) = 0.8$ W; $T_2 = 87$ K; $I_0\left(T_{ref}\right) = 3.6$ A; $T_3 = 1200$ K.

The comparison of Figure 7a,b reveals the limits of the parabolic model for elevated heat sink (active region) temperatures. The description is reasonable up to the roll-over point and for moderate temperature differences relative to the reference temperature (270 K in Figure 7). Beyond these limits the full model (Equation (21)) has to be applied. The variation of the injection efficiency (which is neglected in the parabolic model) with temperature reduces the peak value of the output power and reduces the slope of the P-I curve beyond the maximum. This limitation is acceptable for system-level simulations.

In order to determine the effective thermal resistance of the QCL structure, P-I measurements in high duty-cycle operation at a heatsink temperature of T_{hs} = 293 K were performed. As mentioned before, for this experiment the back facets of the lasers are high-reflectively coated with R ~ 0.8 to enhance the light emission of the front facet, and single-ended emission optical power from only the front facet is counted. The experimental results, together with a simultaneous fit of the parabolic and the thermal models, are depicted in Figure 8. The model parameters had to be adjusted because the threshold current and the peak power adapt themselves to the new resonator configuration. The values are as follows, for a reference temperature of $T_{ref} = 270$ K: $I_{th}\left(T_{ref}\right) = 0.50$ A, $T_0 = 170$ K; $P_{ro}\left(T_{ref}\right) = 1.3$ W; $T_2 = 120$ K. An essential feature of the model states that the Stark scale is determined by the quantum design and, consequently, its parameters should remain same. Please note that the heat sink temperature of the measurements was 293 K.

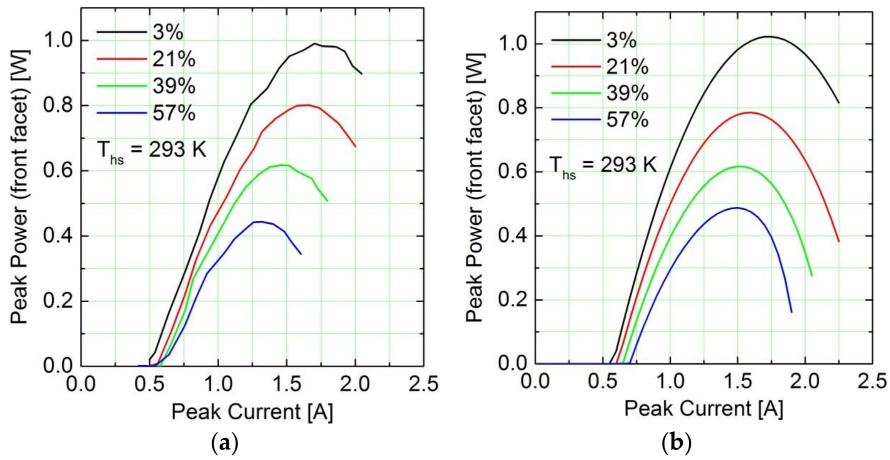

Figure 8. Peak optical output power *vs.* current amplitude in pulsed mode for different duty cycles. The laser is driven by current pulses of 300 ns with various repetition rates. The back facet is HR-coated, optical power from only the front facet has been counted. (**a**) Experimental data; and (**b**) parabolic model fitted to the data.

The electrical input power $U\ I$ to the device above the threshold was calculated from a linear model of the form $U = U_0 + R_s I$ with the parameter values $U_0 = 9.0$ V and $R_s = 3.3\ \Omega$ derived from an analysis of the experimental voltage-current characteristics. We use the same set of parameters independent of the duty cycle. From the data in Figure 8 we estimated an effective thermal resistance of the order $R_{LH} = 7.5$ K/W.

The agreement between experimental and model data is adequate for the purpose of system simulations. Looking at the model data in the light of the limitations mentioned above it is expected that the parabolic approximation is limited to duty cycles up to about 50%.

The variation of the average power as a function of the duty cycle is an electro-optical characteristic of particular interest for applications. This mode of operation allows for the variation of the output power by keeping the amplitude and the duration of the underlying laser pulses fixed. Figure 9 compares the experimental characteristics with the calculated model values. The comparison of both data sets confirms the limits of the parabolic approximation which are observed in Figures 7 and 8.

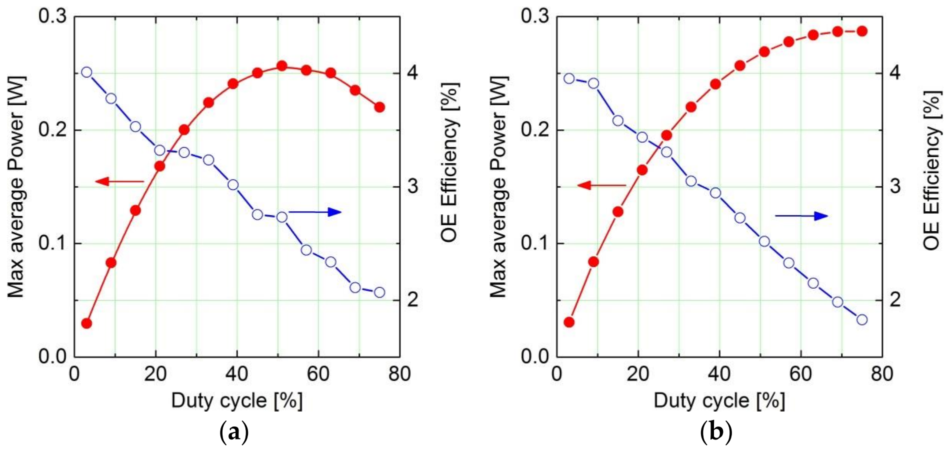

Figure 9. Average optical output power and average power efficiency in pulsed mode *vs.* duty cycle. The laser is driven by current pulses of 300 ns with various repetition rates. The back facet is HR-coated, optical power from only the front facet has been counted. (**a**) Experimental data; and (**b**) calculation based on the parabolic model.

5. Conclusions

Quantum cascade lasers are a versatile technology which opens up new opportunities in civil and defense applications. In order to penetrate different application areas tools are needed which allow the system designer to assess the performance of these new laser sources. In the paper we presented and verified a model for the electro-optical performance of QCL which is based on system physics. This approach links physical processes to model parameters and allows for the exploration of different modes of operation within the limits imposed by physics. It was shown that the model could be reduced to a quadratic dependence of the optical output power on the pump current. In this approximate form, the model parameters need to be calibrated with experimental data. Subsequently, the QCL performance model can be utilized for system-level simulations with acceptable fidelity.

Acknowledgments: The authors express their gratitude to F. Münzhuber and M. Rattunde for discussing the modeling approach and suggesting improvements concerning the presentation of the material. We would like to thank R. Aidam, R. Driad, and W. Bronner who contributed to the fabrication of the QCLs, and R. Ostendorf, C. Schilling, and U. Weinberg who contributed to the characterization of the QCLs.

Author Contributions: H.D.T. did the modeling work and the analysis of the experimental data. Q.Y. contributed the experimental data. Writing the paper was a joint task of all three authors.

Conflicts of Interest: The authors declare no conflict of interest.

Abbreviations

The following abbreviations are used in this manuscript:

DIRCM	Directed Infrared Countermeasures
HR	High Reflective
P-I	Power *vs.* Current
QCL	Quantum Cascade Laser

References

1. Olesberg, J.T.; Flatté, M.E. Theory of mid-wavelength infrared laser active regions: Intrinsic properties and design strategies. In *Mid-Infrared Semiconductor Optoelectronics*; Krier, A., Ed.; Springer-Verlag: London, UK, 2006; pp. 3–92.
2. Jirauschek, C.; Kubis, T. Modeling techniques for quantum cascade lasers. *Appl. Phys. Rev.* **2014**, *1*, 011307. [CrossRef]
3. Faist, J. *Quantum Cascade Laser*; Oxford University Press: Oxford, UK, 2013.
4. Bismuto, A.; Terazzi, R.; Hinkov, B.; Beck, M.; Faist, J. Fully automated quantum cascade laser design by genetic optimization. *Appl. Phys. Lett.* **2012**, *101*, 021103. [CrossRef]
5. Botez, D.; Chang, C.-C.; Mawst, L.J. Temperature sensitivity of the electro-optical characteristics for mid-infrared (λ = 3–16 µm)-emitting quantum cascade lasers. *J. Phys. D Appl. Phys.* **2016**, *49*, 0430. [CrossRef]
6. Botez, D.; Shin, J.C.; Kumar, S.; Kirch, J.; Chang, C.-C.; Mawst, L.J.; Vurgaftman, I.; Meyer, J.R.; Bismuto, A.; Hinkov, B.; *et al.* The temperature dependence of key electro-optical characteristics for mid-infrared emitting quantum cascade lasers. *Proc. SPIE* **2011**. [CrossRef]
7. Flores, Y.V.; Kurlov, S.S.; Elagin, M.; Semtsiv, M.P.; Masselink, W.T. The role of electron temperature in the leakage current in QCLs and its impact on the quantum efficiency. *Proc. SPIE* **2014**. [CrossRef]
8. Yang, Q.K.; Schilling, C.; Ostendorf, R.; Hugger, S.; Fuchs, F.; Wagner, J. Wall-plug efficiency of mid-infrared quantum cascade lasers. *J. Appl. Phys.* **2012**, *111*, 0531111. [CrossRef]
9. Koechner, W. *Solid State Laser Engineering*; Springer Series in Optical Sciences: New York, NY, USA, 2006.
10. Choi, H.; Diehl, L.; Wu, Z.-K.; Giovanni, M.; Faist, J.; Capasso, F.; Norris, T.B. Time resolved investigations of electronic transport dynamics in quantum cascade lasers based on diagonal transition. *IEEE J. Quantum Electron.* **2009**, *45*, 307. [CrossRef]
11. Howard, S.S.; Liu, Z.; Gmachl, C. Thermal and Stark effect roll-over of quantum cascade lasers. *IEEE J. Quantum Electron.* **2008**, *44*, 319. [CrossRef]

12. Vitiello, M.; Gresch, T.; Lops, A.; Spagnolo, V.; Scarmarcio, G.; Hoyler, N.; Giovanni, M.; Faist, J. Influence of InAs, AlAs layers on the optical, electronic, and thermal characteristics of strain-compensated GaInAs/AlInAs quantum-cascade lasers. *Appl. Phys. Lett.* **2007**, *91*, 161111. [CrossRef]
13. Gorfinkel, V.B.; Luryi, S.; Gelmont, B. Theory of gain spectra for quantum cascade lasers and temperature dependence of their characteristics at low and moderate carrier concentrations. *IEEE J. Quantum Electron.* **1996**, *32*. [CrossRef]
14. Maulini, R.; Lyakh, A.; Tsekoun, A.; Patel, C.K.N. λ ~ 7.1 µm quantum cascade lasers with 19% wall-plug efficiency at room temperature. *Opt. Express* **2011**, *19*, 17203. [CrossRef] [PubMed]
15. Tholl, H.D. Modellierung der elektrischen und der elektro-optischen Kennlinien von Quantenkaskadenlasern. Unpublished report. 2015. (In German)
16. Yang, Q.K.; Lösch, R.; Bronner, W.; Hugger, S.; Fuchs, F.; Aidam, R.; Wagner, J. High-peak-power strain-compensated GaInAs/AlInAs quantum cascade lasers (lambda ~ 4.6 µm) based on a slightly-diagonal active region design. *Appl. Phys. Lett.* **2008**, *93*, 251110.